European Journal of Mechanics A/Solids 30 (2011) 770–782

Contents lists available at ScienceDirect

European Journal of Mechanics A/Solids

journal homepage: www.elsevier.com/locate/ejmsol

Analytical modeling of sound transmission through clamped triple-panel partition separated by enclosed air cavities

F.X. Xin, T.J. Lu*

MOE Key Laboratory for Strength and Vibration, School of Aerospace, Xi'an Jiaotong University, Xi'an 710049, PR China

ARTICLE INFO

Article history:
Received 14 December 2010
Accepted 26 April 2011
Available online 6 May 2011

Keywords:
Sound transmission loss
Triple-panel
Clamp supported

ABSTRACT

An analytical model for sound transmission through a clamped triple-panel partition of finite extent and separated by two impervious air cavities is formulated. The solution derived from the model takes the form of that for a clamp supported rectangular plate. A set of modal functions (or more strictly speaking, the basic functions) are employed to account for the clamped boundary conditions, and the application of the virtual work principle leads to a set of simultaneous algebraic equations for determining the unknown modal coefficients. The sound transmission loss (STL) of the triple-panel partition as a function of excitation frequency is calculated and compared with that of a double-panel partition. The model predictions are then used to explore the physical mechanisms associated with the various dips on the STL versus frequency curve, including the equivalent 'mass-spring' resonance, the standing-wave resonance and the panel modal resonance. The asymptotic variation of the solution from a finite-sized partition to an infinitely large partition is illustrated in such a way as to demonstrate the influence of the boundary conditions on the soundproofing capability of the partition. In general, a triple-panel partition outperforms a double-panel partition in insulating the incident sound, and the relatively large number of system parameters pertinent to the triple-panel partition in comparison with that of the double-panel partition offers more design space for the former to tailor its noise reduction performance.

1. Introduction

Recent developments in building, transportation, environmental and other engineering applications have prompted research on finding innovative ways for noise reduction. The transmission loss characteristics of a customarily used single-panel follow in general the mass law. The traditional methods for low-frequency noise reduction require therefore the use of heavy damping materials, leading to weight penalty and hence offsetting the performance gains of the panel. As a result, double-panel partitions are extensively used in modern buildings, transportation vehicles, aerospace/aeronautical fuselages, etc., which have superior sound insulation properties than single-panel partitions (Lyle and Mixson, 1987; Pietrzko and Mao, 2008; Quirt, 1982, 1983; Wu et al., 1997; Xin and Lu, 2010b, 2011a,b; Xin et al., 2009b, 2010). Since the introduction of an additional panel can significantly enhance the transmission loss performance of a single panel, one would expect that a triple-panel partition constructed by adding another panel to the double-panel partition may lead to further gains in noise reduction. As a matter of fact, triple-panel partitions with separated air cavities have already been introduced as the standard configuration for glazing windows in some high-class buildings. We aim therefore in this research to develop an analytical model to investigate the sound transmission loss (STL) performance of a finite-sized triple-panel partition, which is clamp mounted on a rigid baffle and separated by two enclosed air cavities, and compare it with that of a clamped double-panel partition.

A significant amount of research has been devoted to developing accurate theoretical models of STL characteristics for single-panel (Fahy, 1985; Graham, 2007; Langley et al., 1997; Lee and Kim, 2002; Liu et al., 2007; Lomas and Hayek, 1977; Sewell, 1970; Toyoda et al., 2008) and double-panel structures (Beranek and Work, 1949; Lin and Garrelick, 1977; London, 1950; Pietrzko and Mao, 2008; Wang et al., 2005; Xin and Lu, 2009, 2010a, 2010c). Extensive experimental study (Carneal and Fuller, 2004; Quirt, 1982, 1983; Tadeu and Mateus, 2001) has also been carried out and active control strategies (Gardonio, 2002; Gardonio and Elliott, 1999; Kaiser et al., 2003; Sas et al., 1995) for noise reduction proposed.

Early research on interior noise reduction concentrated primarily on infinite structures, because the precise characterization of sound transmission across a finite-sized structure requires complex physical-mathematical treatment of the boundary conditions as well as the fluid-structure coupling effects, and the

* Corresponding author. Tel.: +86 29 82665600; fax: +86 29 83234781.
E-mail address: tjlu@mail.xjtu.edu.cn (T.J. Lu).

0997-7538/$ – see front matter © 2011 Elsevier Masson SAS. All rights reserved.
doi:10.1016/j.euromechsol.2011.04.013

Nomenclature

Roman symbols

a	panel dimension in x-direction
b	panel dimension in y-direction
c_0	sound speed in air
D_i	panel flexural rigidity, $i = 1,2,3$
$\hat{\mathbf{e}}_1$	unit vector in x-direction
$\hat{\mathbf{e}}_2$	unit vector in y-direction
$\hat{\mathbf{e}}_3$	unit vector in z-direction
E_i	Young's modulus, $i = 1,2,3$
f_{mn}	modified natural frequency of simply-supported panel
f_i	resonance frequency of mass-spring system
$f_{s,n}$	standing-wave resonance frequency
$\mathbf{F}$	generalized force vector
H_1	location of second panel in z-direction
H_2	location of third panel in z-direction
$\tilde{H}$	air cavity depth of double-panel
$\tilde{H}_1$	$= H_1$ thickness of bottom air cavity
$\tilde{H}_2$	$= H_2 - H_1$ thickness of top air cavity
h_i^d	thickness of double-panel, $i = 1,2$
h^s	thickness of single-panel
h_i^t	respective thickness of triple-panel, $i = 1,2,3$
I	initial sound amplitude
j	imaginary unit $\sqrt{-1}$
$\mathbf{k}$	wave number vector
k_1	equivalent stiffness of bottom air cavity
k_2	equivalent stiffness of top air cavity
k_x	wave number component in x-direction
k_y	wave number component in y-direction
k_z	wave number component in z-direction
$k_{x,mn}$	$m-n$th wave number component in x-direction
$k_{y,mn}$	$m-n$th wave number component in y-direction
$k_{z,mn}$	$m-n$th wave number component in z-direction
m_i	panel surface density, $i = 1,2,3$
p_α	sound pressure, $\alpha = 1,2,3,4$
q_{mn}	integral constant associated with generalized force
$\mathbf{r}$	position vector
STL	sound transmission loss
t	time
$\mathbf{T}_{11}$	non-zero diagonal sub-matrix (associated with incident panel) of system stiffness matrix
$\mathbf{T}_{12}$	non-zero cross sub-matrix (associated with incident panel) of system stiffness matrix
$\mathbf{T}_{21}$	non-zero cross sub-matrix (associated with middle panel) of system stiffness matrix
$\mathbf{T}_{22}$	non-zero diagonal sub-matrix (associated with middle panel) of system stiffness matrix
$\mathbf{T}_{23}$	non-zero cross sub-matrix (associated with middle panel) of system stiffness matrix
$\mathbf{T}_{32}$	non-zero cross sub-matrix (associated with radiation panel) of system stiffness matrix
$\mathbf{T}_{33}$	non-zero diagonal sub-matrix (associated with radiation panel) of system stiffness matrix
$\hat{\mathbf{u}}_\alpha$	velocity
v_a	local sound speed, $\alpha = 1,2,3,4$
w_i	dynamical panel deflection, $i = 1,2,3$

Greek symbols

α_i	modal coefficient vector, $i = 1,2,3$
$\alpha_{i,mn}$	modal coefficient, $i = 1,2,3$
β_{mn}	$m-n$th reflected wave amplitude
δ	variational symbol
Δ_s^{*t}	pre-defined constant matrix, $s = 1,2$; $t = 1,2,3,4$
ε_{mn}	$m-n$th positive-going wave amplitude in top cavity
ζ_{mn}	$m-n$th negative-going wave amplitude in top cavity
η_{mn}	$m-n$th negative-going wave amplitude in bottom cavity
η_i	panel material loss factor, $i = 1,2,3$
θ	incident azimuth angle
$\lambda_{1,mn}^{*1}$	pre-defined elemental matrix
$\lambda_{1,n}^{*2}$	pre-defined elemental matrix
λ_1^{*3}	pre-defined elemental matrix
λ_2^{*2}	pre-defined elemental matrix
λ_2^{*3}	pre-defined elemental matrix
λ_2^{*4}	pre-defined elemental matrix
$\aleph_1$	$= k_1 m_3 (m_1 + m_2)$
$\aleph_2$	$= k_2 m_1 (m_2 + m_3)$
μ_{mn}	$m-n$th transmitted wave amplitude
ν_i	Poisson ratio, $i = 1,2,3$
ξ_{mn}	$m-n$th positive-going wave amplitude in bottom cavity
Π_α	sound power, $\alpha = 1,2,3,4$
ρ_i	panel material density, $i = 1,2,3$
ρ_0	air density
τ	transmission coefficient
Φ_α	velocity potential of acoustic field, $\alpha = 1,2,3,4$
φ_{mn}	$m-n$th modal function of clamped boundary condition
φ	incident elevation angle
ω	angular frequency

Subscripts

A	panel surface area
i	panel index
m,n	modal order index
M,N	truncation number
$,t$	partial derivative with respect to time
x,y,z	Cartesian coordinates
α	acoustic field index

Superscripts

T	transpose of vector or matrix
$*$	denotation of complex conjugate

evaluation of the finite system response is more difficult due to the presence of violent peaks and dips on STL versus frequency curves.

As far as infinite structures are concerned, Beranek and Work (1949) developed an early model of sound transmission through multiple structures containing flexible blankets based on the progressive impedance method. London (1950) proposed a theory to deal with the transmission of reverberant sound through a double wall, also using the impedance method. The extension of Beranek's model to a random incidence field was carried out by Mulholland et al. (1968). The above mentioned research established on the progressive impedance method failed to fully account for the coincidence effect, which was later overcame by the analytical model of Antonio et al. (2003). An analysis method was developed by Lee and Kim (2002) to study the sound transmission characteristics of a thin plate stiffened by equally spaced line stiffeners in terms of the space harmonic approach. Wang et al. (2005) further applied the space

harmonic approach to periodically connected double-leaf partitions. The transmission of structure-borne sound through a double-leaf structure with a porous absorptive layer inserted in the cavity was studied theoretically as well as experimentally by Yairi et al. (2003), with the porous absorptive layer described using an electro-acoustical equivalent model.

As for the sound transmission across finite-sized structures, several approaches have been employed to account for the edge conditions, such as FEM (finite element method) (Del Coz Diaz et al., 2010; Panneton and Atalla, 1996; Ruzzene, 2004), BEM (boundary element method) (Panneton and Atalla, 1996; Sgard et al., 2000), SEA (statistical energy analysis) (Craik, 2003; Fahy, 1994; Langley et al., 1997; Maidanik, 1962; Price and Crocker, 1970), modal expansion method (Graham, 2007; Leppington et al., 2006; Pietrzko and Mao, 2008), spatial windowing technique (Villot et al., 2001) and patch-mobility method (Chazot and Guyader, 2007). In general, FEM is applied together with BEM to deal with the boundary and interface conditions. For example, for sound transmission through finite multilayer systems containing poroelastic materials, Panneton and Atalla (1996) used the classical elastic and fluid elements to model the elastic and fluid media, but a BEM approach to account for the fluid-structure coupling effects. Sgard et al. (2000) also employed a variational BEM approach to cope with the fluid loading effects. Based on two-dimensional FEM models, Del Coz Diaz et al. (2010) established a methodology to predict the airborne sound insulation of building elements, which agreed well with their experimental measurements. Although FEM and BEM are well suited for low-frequency transmission loss calculations, they require high computation efforts when calculations over a wide frequency range (high frequencies in particular) are needed (Pellicier and Trompette, 2007) and provide few physical insights. Whilst SEA can be used as an alternative of FEM and BEM, for it is substantially more effective in providing sound transmission estimates for complex systems at high frequencies, it is seldom reliable at low frequencies because of the statistical uncertainties that prevail when there are only a few resonant modes present in the subsystems (Leppington et al., 2006; Xin et al., 2008). Furthermore, analogous to FEM and BEM, SEA cannot provide detailed physical understanding of singular phenomena such as resonance. The modal expansion method based on simply-supported edge constraints has been conventionally adopted to solve the vibroacoustic problem of finite systems on account of its excellent capability to deal with resonant modes. However, for clamped boundary conditions, this method is only approximate and needs special treatment for numerical convergence. The spatial windowing technique also suffers from the disadvantage of indeterminate boundary condition disposal and few physical insight gains. The patch-mobility method adopted by Chazot et al. (Chazot and Guyader, 2007) is essentially built upon the modal expansion method.

Although extensive theoretical research on sound transmission through finite and infinite multilayer systems has been carried out, there exists no analytical modeling of sound transmission across a finite-sized triple-panel construction with boundary constraints. A thorough literature search revealed that a few experimental studies (Brekke, 1981; Quirt, 1983; Vinokur, 1990) have concerned the transmission of sound through triple glazing windows. To squarely address this deficiency, the present research aims to develop an analytical model to investigate the detailed process of sound transmission across a clamped triple-panel partition of finite extent and separated by two impervious air cavities. The model is then used to validate one's expectation that a triple-panel partition would possess superior sound insulation properties than the widely used double-panel partition. Specifically, the 'mass-spring' resonance, the standing-wave resonance, the modal behavior of the panel and other interesting vibroacoustic phenomena are identified and interpreted on physical grounds, the asymptotic variation of the transmission loss from finite to infinite extent is illustrated, and a systematic parametrical study regarding the effects of panel thickness and air cavity depth is carried out.

2. Dynamic structural-acoustic formulation

2.1. Geometry and description of triple-panel configuration

We model theoretically the reflection, transmission and radiation of a sound pressure wave propagating through a clamp mounted rectangular triple-panel configuration (Fig. 1), with fluid-structure interaction and coupling effects duly accounted for. The structure is composed of three homogenous and isotropic panels and separated by two enclosed air cavities. A right-handed Cartesian coordinate system (x,y,z) is applied, with the x- and y-axis horizontally located on the surface of the incidence panel (bottom panel) and the z-axis pointing vertically upward, as shown in Fig. 1. In the defined coordinate system, the three panels are indexed as bottom, middle and upper panels having thickness h_1, h_2 and h_3 and located at $z = 0$, H_1 and H_2, respectively (Fig. 1). The rectangular panels have identical dimensions $a \times b$ in the x–y plane. The rigid baffle mounting the triple-panel partition is assumed to be infinitely large so as to exclude possible diffraction of sound around the baffle from the sound source side ($z < 0$) to the sound radiation/transmission side ($z > H_2$).

Under typical fluid-structure interface conditions, the uniform plane sound pressure varying harmonically in time constitutes a basic sound wave incidence on the bottom panel, characterized by the incident elevation angle φ and the incident azimuth angle θ, as shown in Fig. 1. Part of this disturbance is reflected back by the bottom panel, and the rest propagates consecutively through the bottom panel, the bottom cavity, the middle panel and the top cavity to the upper panel, and then is emitted by the vibrating upper panel. The model proposed for the above physical process is based upon the classical vibration theorem for thin flexural plates, which enables the three panels to possess different physical (e.g., Young's modulus, Poisson ratio and loss factor) and geometrical (e.g., length and width) parameters, but requires the panels to be sufficiently thin relative to their length and width so that the shear displacement of a panel is much smaller than its lateral displacement.

2.2. Mathematical formulation and solutions

The acoustic velocity potential for an obliquely incident uniform plane sound wave varying harmonically in time can be expressed as

$$\varphi = Ie^{-j\left(k_x x + k_y y + k_z z - \omega t\right)} \tag{1}$$

where I is the amplitude, $j = \sqrt{-1}$, ω is the angular frequency, and wave number components of the incident sound in x-, y-, and z-directions can be separately calculated as

$$k_x = k_0 \sin\varphi \cos\theta, \quad k_y = k_0 \sin\varphi \sin\theta, \quad k_z = k_0 \cos\varphi \tag{2}$$

here $k_0 = \omega/c_0$ is the wave number in air and c_0 is the sound speed in air.

As noted above, the three panels are modeled as classical thin plates so that, in terms of the thin plate vibration theorem, their motions under sound excitation are governed by:

$$D_1 \nabla^4 w_1 + m_1 \frac{\partial^2 w_1}{\partial t^2} - j\omega\rho_0(\Phi_1 - \Phi_2) = 0 \tag{3}$$

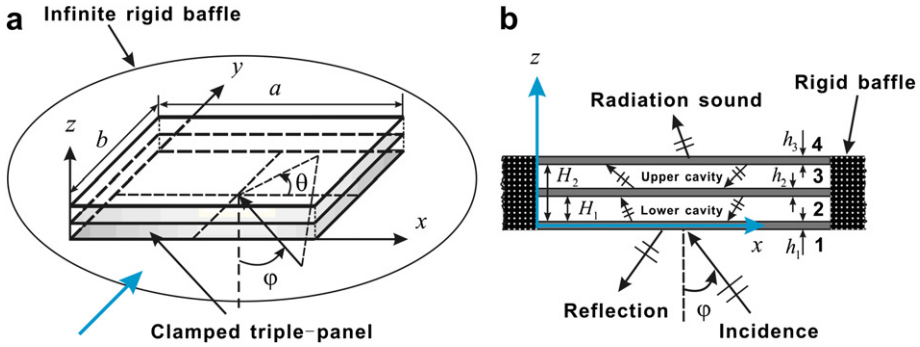

Fig. 1. Schematic of sound transmission through a clamp mounted triple-panel partition: (a) overall view; (b) side view in the arrow direction in (a).

$$D_2\nabla^4 w_2 + m_2\frac{\partial^2 w_2}{\partial t^2} - j\omega\rho_0(\Phi_2 - \Phi_3) = 0 \tag{4}$$

$$D_3\nabla^4 w_3 + m_3\frac{\partial^2 w_3}{\partial t^2} - j\omega\rho_0(\Phi_3 - \Phi_4) = 0 \tag{5}$$

where D_i, m_i and w_i denote separately the panel flexural rigidity, surface density and deflection, with $i = 1,2,3$ representing separately the bottom, middle and top panels, ρ_0 is the air density, and $\Phi_\alpha(\alpha = 1,2,3,4)$ are the velocity potentials in the incident field, in the bottom and top air cavities, and in the transmitted field (Fig. 1), respectively.

In the context of harmonic sound excitation, the transverse displacements of the structure should also be time harmonic, which can be written as

$$w_i(x,y;t) = \sum_{m,n}\alpha_{i,mn}\varphi_{mn}(x,y)e^{j\omega t} \quad (i = 1,2,3) \tag{6}$$

where the modal functions (or, more strictly speaking, the basic functions) φ_{mn} take the following forms (Leissa, 1993; Taylor and Govindjee, 2004; Xin et al., 2009a)

$$\varphi_{mn}(x,y) = \left(1 - \cos\frac{2m\pi x}{a}\right)\left(1 - \cos\frac{2n\pi y}{b}\right) \tag{7}$$

The velocity potentials of the acoustic field are associated with the local velocity by $\hat{\mathbf{u}}_\alpha = -\nabla\Phi_\alpha$, and related to the acoustic pressure by $p_\alpha = \rho_0\Phi_{\alpha,t} = j\omega\rho_0\Phi_\alpha$. The velocity potentials can be described in terms of the modal function φ_{mn}, as:

$$\Phi_1(\mathbf{r};t) = \sum_{m,n} I_{mn}\varphi_{mn}(x,y)e^{-j(k_z z-\omega t)} + \sum_{m,n}\beta_{mn}\varphi_{mn}(x,y)e^{-j(-k_z z-\omega t)} \tag{8}$$

$$\Phi_2(\mathbf{r};t) = \sum_{m,n}\varepsilon_{mn}\varphi_{mn}(x,y)e^{-j(k_z z-\omega t)} + \sum_{m,n}\zeta_{mn}\varphi_{mn}(x,y)e^{-j(-k_z z-\omega t)} \tag{9}$$

$$\Phi_3(\mathbf{r};t) = \sum_{m,n}\xi_{mn}\varphi_{mn}(x,y)e^{-j(k_z z-\omega t)} + \sum_{m,n}\eta_{mn}\varphi_{mn}(x,y)e^{-j(-k_z z-\omega t)} \tag{10}$$

$$\Phi_4(\mathbf{r};t) = \sum_{m,n}\mu_{mn}\varphi_{mn}(x,y)e^{-j(k_z z-\omega t)} \tag{11}$$

where I_{mn} stands for the amplitudes of the incident sound wave, β_{mn} represents the amplitude of the reflected sound waves, $\varepsilon_{mn}(\xi_{mn})$ and $\zeta_{mn}(\eta_{mn})$ denote the amplitudes of the positive- and negative-going waves in the bottom and top cavities, respectively; μ_{mn} is the amplitudes of transmitted waves (i.e., the positive-going waves) in the transmitted domain (see Fig. 1).

On the premise that the considered vibroacoustic problem involves fluid–structure interaction and mutual coupling, the velocity continuity condition (equivalent to the displacement continuity condition when the surrounding fluid is stationary with respect to the structure (Ingard, 1959)) should be satisfied at the fluid–structure interface, so that:

$$z = 0; \quad -\frac{\partial\Phi_1}{\partial z} = j\omega w_1, \quad -\frac{\partial\Phi_2}{\partial z} = j\omega w_1 \tag{12}$$

$$z = H_1; \quad -\frac{\partial\Phi_2}{\partial z} = j\omega w_2, \quad -\frac{\partial\Phi_3}{\partial z} = j\omega w_2 \tag{13}$$

$$z = H_2; \quad -\frac{\partial\Phi_3}{\partial z} = j\omega w_3, \quad -\frac{\partial\Phi_4}{\partial z} = j\omega w_3 \tag{14}$$

Substitution of Eq. (6) and Eqs. (8)–(11) into the above velocity continuity conditions leads to a set of simultaneous equations for the unknown coefficients β_{mn}, ε_{mn}, ζ_{mn}, ξ_{mn}, η_{mn}, μ_{mn}, as:

$$-Ie^{-j(k_x x+k_y y)} + \sum_{m,n}\left[\beta_{mn} + \frac{\omega}{k_z}\alpha_{1,mn}\right]\times\varphi_{mn}(x,y) = 0 \tag{15}$$

$$\sum_{m,n}\left[k_z(-\varepsilon_{mn} + \zeta_{mn}) + \omega\alpha_{1,mn}\right]\times\varphi_{mn}(x,y) = 0 \tag{16}$$

$$\sum_{m,n}\left[k_z\left(-\varepsilon_{mn}e^{-jk_z H_1} + \zeta_{mn}e^{jk_z H_1}\right) + \omega\alpha_{2,mn}\right]\times\varphi_{mn}(x,y) = 0 \tag{17}$$

$$\sum_{m,n}\left[k_z\left(-\xi_{mn}e^{-jk_z H_1} + \eta_{mn}e^{jk_z H_1}\right) + \omega\alpha_{2,mn}\right]\times\varphi_{mn}(x,y) = 0 \tag{18}$$

$$\sum_{m,n}\left[k_z\left(-\xi_{mn}e^{-jk_z H_2} + \eta_{mn}e^{jk_z H_2}\right) + \omega\alpha_{3,mn}\right]\times\varphi_{mn}(x,y) = 0 \tag{19}$$

$$\sum_{m,n}\left[-k_z\mu_{mn}e^{-jk_z H_2} + \omega\alpha_{3,mn}\right]\times\varphi_{mn}(x,y) = 0 \tag{20}$$

Since the above simultaneous equations are valid at all values of x and y, they can be further simplified [except Eq. (15)], as:

$$\varepsilon_{mn} = \frac{\omega\left(\alpha_{1,mn}e^{2jk_zH_1} - \alpha_{2,mn}e^{jk_zH_1}\right)}{k_z\left(e^{2jk_zH_1}-1\right)} \tag{21}$$

$$\zeta_{mn} = \frac{\omega\left(\alpha_{1,mn} - \alpha_{2,mn}e^{jk_zH_1}\right)}{k_z\left(e^{2jk_zH_1}-1\right)} \tag{22}$$

$$\xi_{mn} = \frac{\omega\left(\alpha_{3,mn}e^{jk_zH_1} - \alpha_{2,mn}e^{jk_zH_2}\right)}{k_z\left(e^{jk_z(H_1-H_2)} - e^{jk_z(H_2-H_1)}\right)} \tag{23}$$

$$\eta_{mn} = \frac{\omega\left(\alpha_{3,mn}e^{-jk_zH_1} - \alpha_{2,mn}e^{-jk_zH_2}\right)}{k_z\left(e^{jk_z(H_1-H_2)} - e^{jk_z(H_2-H_1)}\right)} \tag{24}$$

$$\mu_{mn} = \frac{\omega\alpha_{3,mn}e^{jk_zH_2}}{k_z} \tag{25}$$

2.2.1. The principle of virtual work

To determine the unknown modal coefficients $\alpha_{1,mn}$, $\alpha_{2,mn}$ and $\alpha_{3,mn}$, the principle of virtual work is employed. The work exerted by the force on each particle that acts through an arbitrary virtual displacement (i.e., an arbitrary infinitesimal change in the position of the particle consistent with the constraints imposed on the motion of the particle) is given by:

$$\delta w_i = \delta\alpha_{i,mn}\varphi_{mn}(x,y) \quad (i = 1,2,3) \tag{26}$$

Summing the above for the system gives the virtual work that must equal zero. For the present problem, the principle of virtual work in the weak form can be specified as:

$$\iint_A\left[D_1\nabla^4 w_1 + m_1\frac{\partial^2 w_1}{\partial t^2} - j\omega\rho_0(\Phi_1-\Phi_2)\right]\cdot\delta w_1 \mathrm{d}A = 0 \tag{27}$$

$$\iint_A\left[D_2\nabla^4 w_2 + m_2\frac{\partial^2 w_2}{\partial t^2} - j\omega\rho_0(\Phi_2-\Phi_3)\right]\cdot\delta w_2 \mathrm{d}A = 0 \tag{28}$$

$$\iint_A\left[D_3\nabla^4 w_3 + m_3\frac{\partial^2 w_3}{\partial t^2} - j\omega\rho_0(\Phi_3-\Phi_4)\right]\cdot\delta w_3 \mathrm{d}A = 0 \tag{29}$$

Upon substitution of Eqs. (6)–(11) and (26) into Eqs. (27)–(29) and, with the help of Eqs. (15) and (21)–(25), three infinite systems of equations are obtained, which can be solved simultaneously by truncation, as demonstrated below.

2.2.2. Determination of modal coefficients

Finally, following the procedures outlined in the preceding section and after some laborious but straightforward algebraic manipulations, three infinite systems of simultaneous algebraic equations for the unknown coefficients $\alpha_{1,mn}$, $\alpha_{2,mn}$ and $\alpha_{3,mn}$ can be obtained, as:

$$\begin{aligned}
&4D_1\pi^4 ab\left\{\left[3\left(\frac{m}{a}\right)^4 + 3\left(\frac{n}{b}\right)^4 + 2\left(\frac{m}{a}\right)^2\left(\frac{n}{b}\right)^2\right]\alpha_{1,mn}\right.\\
&\left.+\sum_{k\neq m}2\left(\frac{n}{b}\right)^4\alpha_{1,kn} + \sum_{l\neq n}2\left(\frac{m}{a}\right)^4\alpha_{1,ml}\right\}\\
&+\frac{9ab}{4}\left[-m_1\omega^2\alpha_{1,mn} + j\omega\rho_0\left(\frac{\omega}{k_z}\alpha_{1,mn} + \varepsilon_{mn} + \zeta_{mn}\right)\right]\\
&+\frac{3ab}{2}\sum_{k\neq m}\left[-m_1\omega^2\alpha_{1,kn} + j\omega\rho_0\left(\frac{\omega}{k_z}\alpha_{1,kn} + \varepsilon_{kn} + \zeta_{kn}\right)\right]\\
&+\frac{3ab}{2}\sum_{l\neq n}\left[-m_1\omega^2\alpha_{1,ml} + j\omega\rho_0\left(\frac{\omega}{k_z}\alpha_{1,ml} + \varepsilon_{ml} + \zeta_{ml}\right)\right]\\
&+ab\sum_{k\neq m,l\neq n}\left[-m_1\omega^2\alpha_{1,kl} + j\omega\rho_0\left(\frac{\omega}{k_z}\alpha_{1,kl} + \varepsilon_{kl} + \zeta_{kl}\right)\right]\\
&= 2j\omega\rho_0 Iq_{mn}(k_x,k_y)
\end{aligned} \tag{30}$$

$$\begin{aligned}
&4D_2\pi^4 ab\left\{\left[3\left(\frac{m}{a}\right)^4 + 3\left(\frac{n}{b}\right)^4 + 2\left(\frac{m}{a}\right)^2\left(\frac{n}{b}\right)^2\right]\alpha_{2,mn}\right.\\
&\left.+\sum_{k\neq m}2\left(\frac{n}{b}\right)^4\alpha_{2,kn} + \sum_{l\neq n}2\left(\frac{m}{a}\right)^4\alpha_{2,ml}\right\}\\
&+\frac{9ab}{4}\left\{-m_2\omega^2\alpha_{2,mn} - j\omega\rho_0\left[(\varepsilon_{mn}-\xi_{mn})e^{-jk_zH_1}\right.\right.\\
&\left.\left.+(\zeta_{mn}-\eta_{mn})e^{jk_zH_1}\right]\right\} + \frac{3ab}{2}\sum_{k\neq m}\left\{-m_2\omega^2\alpha_{2,kn}\right.\\
&\left.-j\omega\rho_0\left[(\varepsilon_{kn}-\xi_{kn})e^{-jk_zH_1} + (\zeta_{kn}-\eta_{kn})e^{jk_zH_1}\right]\right\}\\
&+\frac{3ab}{2}\sum_{l\neq n}\left\{-m_2\omega^2\alpha_{2,ml} - j\omega\rho_0\left[(\varepsilon_{ml}-\xi_{ml})e^{-jk_zH_1}\right.\right.\\
&\left.\left.+(\zeta_{ml}-\eta_{ml})e^{jk_zH_1}\right]\right\} + ab\sum_{k\neq m,l\neq n}\left\{-m_2\omega^2\alpha_{2,kl}\right.\\
&\left.-j\omega\rho_0\left[(\varepsilon_{kl}-\xi_{kl})e^{-jk_zH_1} + (\zeta_{kl}-\eta_{kl})e^{jk_zH_1}\right]\right\} = 0
\end{aligned} \tag{31}$$

$$\begin{aligned}
&4D_3\pi^4 ab\left\{\left[3\left(\frac{m}{a}\right)^4 + 3\left(\frac{n}{b}\right)^4 + 2\left(\frac{m}{a}\right)^2\left(\frac{n}{b}\right)^2\right]\alpha_{3,mn}\right.\\
&\left.+\sum_{k\neq m}2\left(\frac{n}{b}\right)^4\alpha_{3,kn} + \sum_{l\neq n}2\left(\frac{m}{a}\right)^4\alpha_{3,ml}\right\}\\
&+\frac{9ab}{4}\left\{-m_3\omega^2\alpha_{3,mn} - j\omega\rho_0\left[(\xi_{mn}-\mu_{mn})e^{-jk_zH_2}\right.\right.\\
&\left.\left.+\eta_{mn}e^{jk_zH_2}\right]\right\} + \frac{3ab}{2}\sum_{k\neq m}\left\{-m_3\omega^2\alpha_{3,kn} - j\omega\rho_0\right.\\
&\left.\times\left[(\xi_{kn}-\mu_{kn})e^{-jk_zH_2} + \eta_{kn}e^{jk_zH_2}\right]\right\} + \frac{3ab}{2}\sum_{l\neq n}\\
&\left\{-m_3\omega^2\alpha_{3,ml} - j\omega\rho_0\left[(\xi_{ml}-\mu_{ml})e^{-jk_zH_2} + \eta_{ml}e^{jk_zH_2}\right]\right\}\\
&+ab\sum_{k\neq m,l\neq n}\left\{-m_3\omega^2\alpha_{3,kl} - j\omega\rho_0\left[(\xi_{kl}-\mu_{kl})e^{-jk_zH_2}\right.\right.\\
&\left.\left.+\eta_{kl}e^{jk_zH_2}\right]\right\} = 0
\end{aligned} \tag{32}$$

where the abbreviation $\sum_{k\neq m}$ (or $\sum_{l\neq n}$) has the conventional meaning that summation is intended with the index k (or l) taking integer values from 1 to $+\infty$ except for the specified value m (or n). Similarly, the notation $\sum_{k\neq m,l\neq n}$ denotes double summation about indices

k and l from 1 to $+\infty$ apart from the prescribed values m and n. Additionally, a parameter associated with the generalized force F (see Appendix A for details) appears during the process of integration, as:

$$q_{mn}(k_x,k_y) = \begin{cases} ab & k_x = 0 \text{ and } k_y = 0 \\ \dfrac{4jn^2\pi^2 a\left(1-e^{-jk_y b}\right)}{k_y\left(k_y^2 b^2 - 4n^2\pi^2\right)} & k_x = 0 \text{ and } k_y \neq 0 \\ \dfrac{4jm^2\pi^2 b\left(1-e^{-jk_x a}\right)}{k_x\left(k_x^2 a^2 - 4m^2\pi^2\right)} & k_x \neq 0 \text{ and } k_y = 0 \\ -\dfrac{16m^2n^2\pi^4\left(1-e^{-jk_x a}\right)\left(1-e^{-jk_y b}\right)}{k_x k_y\left(k_x^2 a^2 - 4m^2\pi^2\right)\left(k_y^2 b^2 - 4n^2\pi^2\right)} & k_x \neq 0 \text{ and } k_y \neq 0 \end{cases} \tag{33}$$

In terms of matrix formulation, Eqs. (30)–(32) can be rewritten as a linear system of equations consisting of $3MN$ equilibrium equations by taking truncation of m from 1 to M and n from 1 to N, as:

$$\begin{bmatrix} \mathbf{T}_{11} & \mathbf{T}_{12} & 0 \\ \mathbf{T}_{21} & \mathbf{T}_{22} & \mathbf{T}_{23} \\ 0 & \mathbf{T}_{32} & \mathbf{T}_{33} \end{bmatrix}_{3MN\times 3MN} \begin{Bmatrix} \boldsymbol{\alpha}_1 \\ \boldsymbol{\alpha}_2 \\ \boldsymbol{\alpha}_3 \end{Bmatrix}_{3MN\times 1} = \begin{Bmatrix} \mathbf{F} \\ 0 \\ 0 \end{Bmatrix}_{3MN\times 1} \tag{34}$$

where $\mathbf{T}_{11}$, $\mathbf{T}_{12}$ are the vectors derived from Eq. (30) that correspond to the unknown modal coefficient vector $\boldsymbol{\alpha}_1$; $\mathbf{T}_{21}$, $\mathbf{T}_{22}$, $\mathbf{T}_{23}$ are the vectors arising from Eq. (31) that relate to the unknown modal coefficient vector $\boldsymbol{\alpha}_2$; and the vectors $\mathbf{T}_{32}$ and $\mathbf{T}_{33}$ are derived from Eq. (32) with respect to $\boldsymbol{\alpha}_3$. More details can be found in Appendix A.

2.3. Sound transmission loss

The sound power of the relevant acoustic fields ($\alpha = 1,2,3,4$; see Fig. 1) can be defined as (Chazot and Guyader, 2007; Panneton and Atalla, 1996):

$$\prod_\alpha = \frac{1}{2}\,\mathrm{Re}\iint_A p_\alpha \cdot v_\alpha^* \mathrm{d}A \tag{35}$$

where the local volume velocity is related to the sound pressure through the impendence of air as $v_\alpha = p_\alpha/(\rho_0 c_0)$, and the superscript asterisk denotes complex conjugate.

The transmission coefficient is defined as the ratio of the transmitted sound power to the incident sound power:

$$\tau(\varphi,\theta) = \frac{\Pi_4}{\Pi_1} \tag{36}$$

which is dependent upon the incident angles φ and θ. The sound transmission loss (STL) is then customarily defined as the inverse of the power transmission coefficient in decibels scale, as:

$$\mathrm{STL} = 10\,\log_{10}\left(\frac{1}{\tau}\right) \tag{37}$$

Throughout the present study, STL is used as a measure of the effectiveness of a clamped triple-panel (or, for comparison, double-panel) configuration of finite extent in isolating the incident sound.

3. Numerical results and discussion

Due to the presence of additional panel and air cavity, the acoustic insulation behavior of a triple-panel partition is expected to contain considerably richer physical details than those of a double-panel partition. A set of numerical calculations with the present analytical model is carried out below to quantify the transmission loss characteristics of a clamp supported triple-panel partition and explore the underlying physical mechanisms. To understand the main features of the overall system, the sound transmission performance of an infinitely large triple-panel partition is firstly investigated; subsequently, the comparison between single- and triple-panel partitions aims to understand the different modal behaviors of sound transmission through the two different structures; finally, the performance of the triple-panel is compared with that of a double-panel for different cases.

3.1. Model validation

The validity and feasibility of the proposed theoretical model for sound transmission across triple-panel partitions is checked by comparing model predictions with existing experiment results (Brekke, 1981), as shown in Fig. 2. In the present simulation, sound transmission loss (STL) is calculated in 1/3 octave bands with a diffuse field integration. Overall, as illustrated in Fig. 2, the present theoretical results agree excellently with those measured. The small discrepancies may be attributed to the fact that the mineral wool filled around the edges of the partition in factual measurement is not accounted for in the model.

3.2. Sound transmission characteristics of triple-panel structure

3.2.1. Physical interpretation of STL dips

To exclude the panel modal behavior due to edge constraints, Fig. 3 shows separately the characteristics of normal incident transmission loss through a single-, double- and triple-panel partition of infinite extent. As anticipated, the STL versus frequency curve of the single-panel obeys the mass law, while a set of dips appear on the STL versus frequency curves of double- and triple-panel partitions at frequencies related to the system resonance mode. Note that similar plots for double-panel partitions have been presented in our previous work. With special focus placed upon the STL versus frequency curve of the triple-panel partition, it is observed that within the frequency range considered, two different kinds of resonance exist, i.e., those associated with the first and second dips labeled by the symbol ◆, and subsequent dips at higher frequencies labeled by the symbol ▲.

Analogous to the 'mass–air–mass' resonance of a double-panel system, the triple-panel partition can also be simplified as a system

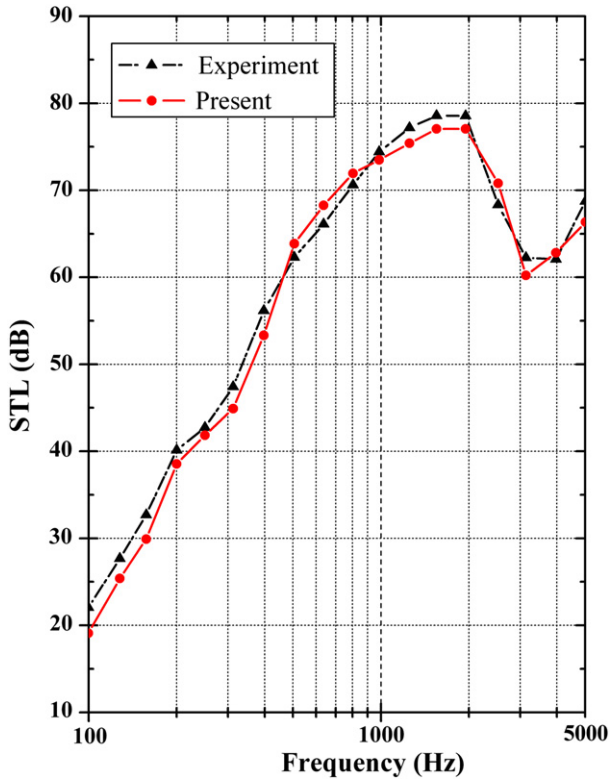

Fig. 2. Diffuse sound transmission loss (STL) plotted as a function of incident frequency: comparison between present model predictions with experimental measurements (Brekke, 1981).

of three lumped masses (m_1, m_2 and m_3) connected together by two springs with stiffness k_1 and k_2, respectively. In the case of sound incident normally to the partition, the eigenvalue equation of this simplified mass-spring system can be written as:

$$|\mathbf{K}-\omega^2\mathbf{M}| = \begin{vmatrix} k_1-\omega^2 m_1 & -k_1 & 0 \\ -k_1 & k_1+k_2-\omega^2 m_2 & -k_2 \\ 0 & -k_2 & k_2-\omega^2 m_3 \end{vmatrix} = 0 \quad (38)$$

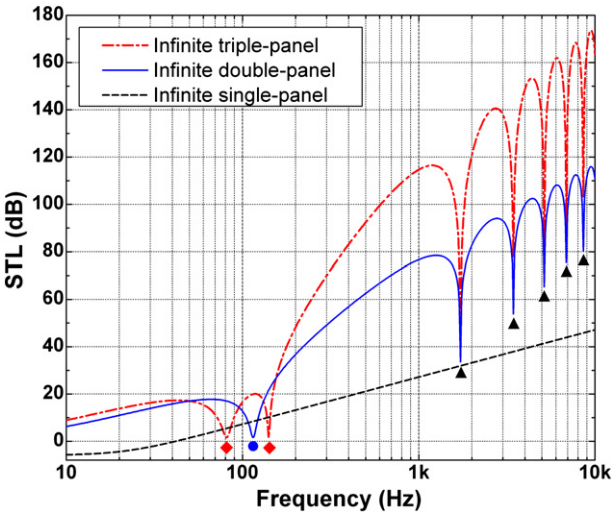

Fig. 3. Comparison of STL versus frequency curves amongst infinite single-, double- and triple-panel partitions ($h^s = 0.002$ m for single-panel; $\tilde{H} = 0.1$ m, $h_1^d = h_2^d = 0.002$ m for double-panel; $\tilde{H}_1 = \tilde{H}_2 = 0.1$ m, $h_1^t = h_2^t = h_3^t = 0.002$ m for triple-panel). Symbols: ● mass–air–mass resonance; ◆ mass–air–mass–air–mass resonance; ▲ standing-wave resonance.

from which the resonance frequencies of the equivalent mass-spring system can be obtained, as:

$$f_1 = \frac{\sqrt{2}}{4\pi}\sqrt{\frac{\lambda_1+\lambda_2-\sqrt{(\lambda_1-\lambda_2)^2+4k_1k_2m_1^2m_3^2}}{m_1m_2m_3}} \quad (39)$$

$$f_2 = \frac{\sqrt{2}}{4\pi}\sqrt{\frac{\lambda_1+\lambda_2+\sqrt{(\lambda_1-\lambda_2)^2+4k_1k_2m_1^2m_3^2}}{m_1m_2m_3}} \quad (40)$$

Here, $\lambda_1 = k_1m_3(m_1+m_2)$ and $\lambda_2 = k_2m_1(m_2+m_3)$, with $k_i = \rho_0c_0^2/\tilde{H}_i$ $(i = 1,2)$, are the equivalent stiffness of the lower air cavity and the upper air cavity, respectively. The introduction of the additional panel and air cavity induces more complicated fluid-structural coupling in the triple-panel system. As a result, one dip corresponding to the 'mass–air–mass' resonance of the double-panel system is divided into two dips for the triple-panel system. The two formulas (39) and (40) can be used to estimate the resonance frequencies associated with the two dips, which have been specially labeled by symbol ◆ in Fig. 3.

At larger frequencies, the resonance dips denoted by symbol ▲ in Fig. 3 are associated with the standing-wave resonance phenomenon due to the interaction effect of successively reflected waves inside the air cavity. For such phenomenon to occur, the depth of the air cavity should be integer numbers of the half wavelength of the incident sound. The n-th standing-wave resonances occurs therefore at the frequency (Wang et al., 2005):

$$f_{s,n} = \frac{nc_0}{2\tilde{H}} \quad (n = 1,2,3\ldots) \quad (41)$$

where $\tilde{H}$ is the depth of the air cavity having a value of 0.1 m for both the double- and triple-panel systems considered. In accordance with the prediction of (41), the standing-wave resonance frequencies should be the same for the two systems, which is confirmed by the excellent agreement shown in Fig. 3 for frequencies above 1 kHz.

The predictions of the present theory for the resonance frequencies of an infinite triple-panel partition are compared in Table 1 with those of the closed-formulas, i.e., Eqs. (39)–(41). Excellent agreement is achieved, suggesting that the theoretical modeling is consistent with the above stated physical nature of the STL dips.

For a clamp supported triple-panel partition of finite extent, the modal behavior of the panel plays a dominant role in the appearance of numerous resonance dips on the STL versus frequency curve, as shown in Fig. 4. To clearly identify the resonance dips induced by the panel natural vibratory modes, the STL versus frequency curves of the single- and double-panels are plotted together with that of the triple-panel. It is seen from Fig. 4 that the first dips associated with the three partitions agree well with each other, while other dips associated with the panel vibratory modes achieve good agreement only between the double- and triple-panel

Table 1
Comparison between theory and closed-form formulas for resonance frequencies of infinite triple-panel partition.

Order	Mass-spring resonance f_i (Hz)		Standing-wave resonance $f_{s,n}$ (Hz)	
	Theory	Eqs. (39) and (40)	Theory	Eq. (41)
1	81.20	81.72	1719	1715
2	140.89	141.54	3436	3430
3	\	\	5146	5145
4	\	\	6863	6860

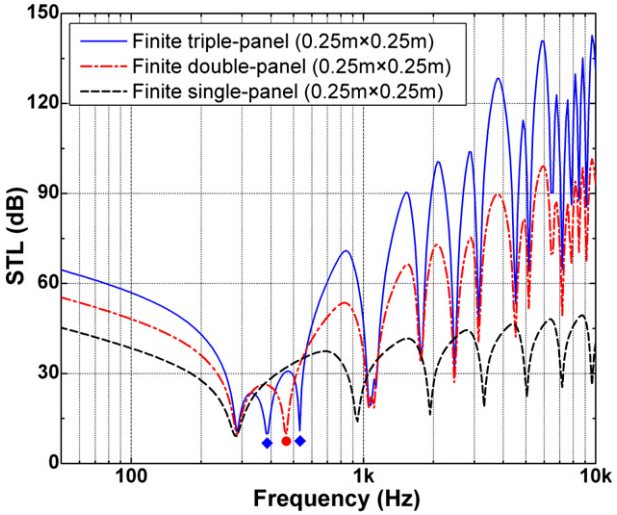

Fig. 4. Comparison of *STL* versus frequency curves amongst clamp supported rectangular single-, double- and triple-panel partitions (h^s = 0.002 m for single-panel; $\bar{H}$ = 0.010 m, $h_1^d = h_2^d$ = 0.002 m for double-panel; $\bar{H}_1 = \bar{H}_2$ = 0.010 m, $h_1^t = h_2^t = h_3^t$ = 0.002 m for triple-panel). Symbols: ● mass–air–mass resonance; ◆ mass–air–mass–air–mass resonance.

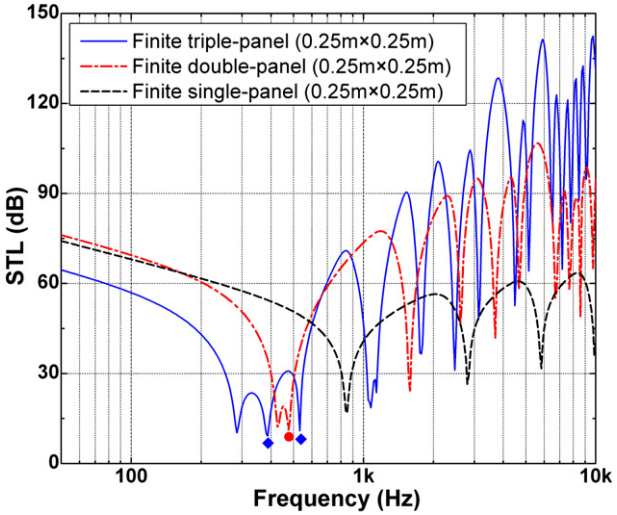

Fig. 5. Comparison of *STL* versus frequency curves amongst clamp supported rectangular single-, double- and triple-panel partitions (h^s = 0.006 m for single-panel; $\bar{H}$ = 0.020 m, $h_1^d = h_2^d$ = 0.003 m for double-panel; $\bar{H}_1 = \bar{H}_2$ = 0.010 m, $h_1^t = h_2^t = h_3^t$ = 0.002 m for triple-panel). Symbols: ● mass–air–mass resonance; ◆ mass–air–mass–air–mass resonance.

partitions, which deviate away from those of the single-panel partition. This is caused by the air cavity coupling effect that is absent in the single-panel system. Moreover, several additional dips appear on the STL frequency curves of double- and triple-panel partitions due to the mass-spring resonance and standing-wave resonance.

Built upon the results for simply-supported boundary conditions, the frequencies corresponding to the STL dips arising from panel vibratory modes in clamp supported double- and triple-panel partitions can be approximately estimated by:

$$f_{mn} = \frac{\pi}{2}\left(\frac{m^2}{a^2}+\frac{n^2}{b^2}\right)\sqrt{\frac{\sqrt{2}Eh^2}{12\rho(1-\nu^2)}} \tag{42}$$

3.2.2. Comparison amongst single-, double- and triple-panel partitions with equivalent total mass

As illustrated in Fig. 4, for relatively high frequencies exceeding the mass-spring resonance frequency, improved sound insulation is demonstrated for triple-panel partitions over single- and double-panel partitions. However, an increase of STL would be expected simply from the mass increase resulting from the addition of a third panel. To provide a fair comparison, theoretical results for the three configurations (i.e., single-, double- and triple-panel partitions) with equivalent total mass are plotted in Fig. 5.

In comparison, the STL dips induced by the mass-spring resonance deviate much amongst different structures, due mainly to the different panel masses and air cavity coupling effects. In the frequency range above the mass-spring resonance frequency, on the whole a triple-panel partition provides larger STL than a double-panel partition and remarkably larger STL than a single-panel partition. This suggests that cavity-coupling effects play a dominant role in this frequency range for double- and triple-panel partitions. In contrast, in the frequency range below the mass-spring resonance frequency, the triple-panel partition exhibits poorer sound insulation than both single- and double-panel partitions. In other words, multi-panel partitions do not provide improved soundproofing capability than single panels with equivalent mass in frequencies below the mass-spring resonance frequency, implying that cavity coupling of multi-panel partitions has little effect on STL in the low-frequency range.

For frequencies below the cut-off frequency for the cavities, the present theoretical results as discussed above are completely in accordance with the experimental results of Brekke (1981) for double- and triple-panel partitions.

3.3. Parametrical study for clamp supported triple-panel partitions

3.3.1. Asymptotic variation of STL versus frequency curve from finite to infinite system

To examine the variation of the transmission loss characteristics of a triple-panel partition with varying geometrical dimensions, two selected finite cases (i.e., 0.25 m × 0.25 m and 0.5 m × 0.5 m) are compared in Fig. 6 with the infinite case, with the air cavity depth fixed at 0.010 m. It is seen from Fig. 6 that, as the panel dimensions increase, the panel-mode-dominated STL dips are

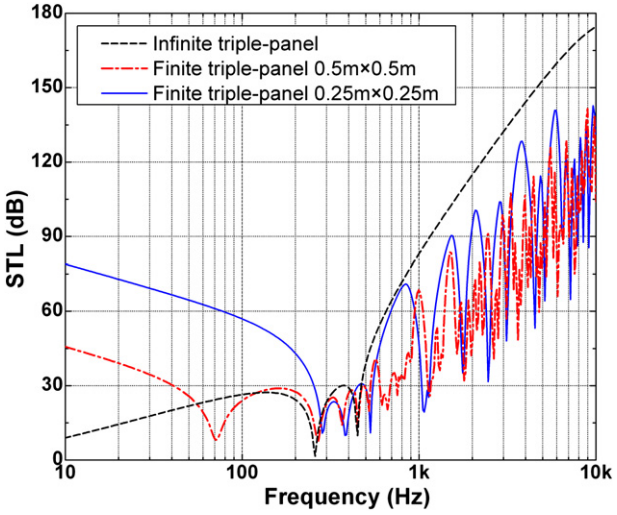

Fig. 6. Variation of sound transmission loss with panel dimensions for triple-panel partitions ($\bar{H}_1 = \bar{H}_2$ = 0.010 m, $h_1^t = h_2^t = h_3^t$ = 0.002 m).

shifted toward the lower frequencies, which are consistent with the predictions of Eq. (42). Beyond the mass-spring resonance dip, the STL versus frequency curve of the infinite triple-panel structure sets upper bound for the finite-sized partitions, because the panel-mode-dominated STL dips vanish in the infinite case. At frequencies below the mass-spring dip, however, the soundproofing performance of the infinite structure is significantly inferior to that of finite-sized structures due to boundary constraint effects. Actually, this trend is mainly affected by the (1,1) panel mode resonance dips for different panel geometrical dimensions. As can be seen in Eq. (42), the (1, 1) panel mode resonance frequency decreases with increasing panel dimensions, which are separately associated with the first dip for the two finite cases and the dip at 0 Hz for the infinite case. Also, for the same reason, the soundproofing capability of the triple-panel partition increases with decreasing panel dimensions. Since for many applications, noise reduction at the low-frequency range (<500 Hz) is of vital importance, this finding has significant implications on the practical design of triple-panel partitions such as the soundproofing windows installed in high-class buildings and aircraft fuselages.

3.3.2. *Effects of panel thickness*

To demonstrate how the sound transmission performance of a triple-panel partition varies with panel thickness, the STL versus frequency curves for the infinite case are plotted in Figs. 7 and 8 whilst those for the finite case are presented in Figs. 9 and 10. As shown in Fig. 7, the STL value is increased significantly as the panel thickness is increased, which is consistent with the mass law for a single panel but more noticeable due to cavity coupling effects. The mass-spring resonance dips shift downward as the panel thickness is increased, due to the increased surface density of the panel. The standing-wave resonance dips reside in their original locations, however, implying that these are independent of the panel thickness.

To highlight the different roles played by the three panels in the sound transmission process, the thicknesses of arbitrarily selected two panels are fixed whilst that of the remaining one is systematically varied. The results for a triple-panel partition of infinite extent are firstly presented in Fig. 8, and it is seen that the increased thickness of any panel amongst the three leads to the increase in STL. The good agreement between Fig. 8(a) and 8(c) suggests the same role played by the incident panel and the radiation panel, which completely follows the acoustical reciprocal theorem. The mass-spring resonance dips shift in a distinct way as the thickness of the middle panel is increased [Fig. 8(b)], which is in accordance with the predictions of Eqs. (39) and (40).

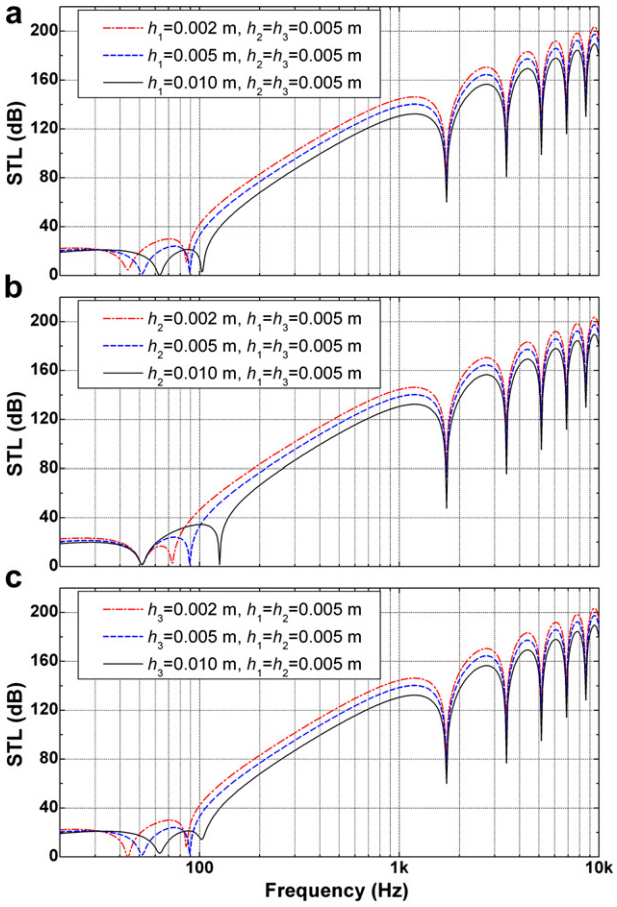

Fig. 8. Variation of STL for infinite triple-panel partition ($\tilde{H}_1 = \tilde{H}_2 = 0.1$ m) under normal sound excitation with the thickness of: (a) incident panel; (b) middle panel; (c) radiation panel.

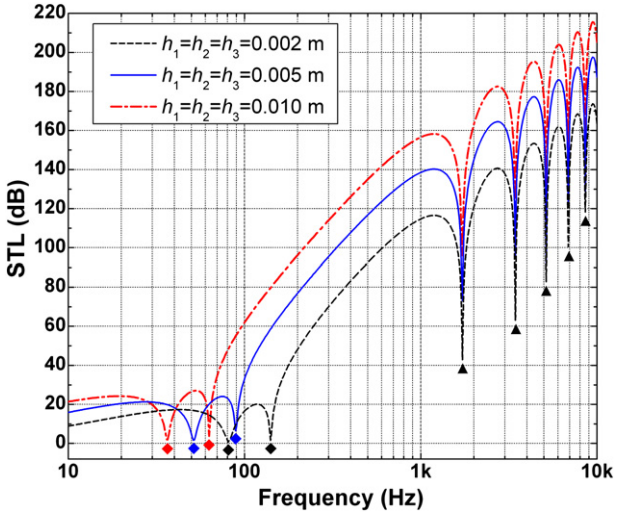

Fig. 7. Effects of panel thickness on STL for infinite triple-panel partition ($\tilde{H}_1 = \tilde{H}_2 = 0.1$ m) under normal sound excitation: ◆ mass–air–mass–air–mass resonance; ▲ standing-wave resonance.

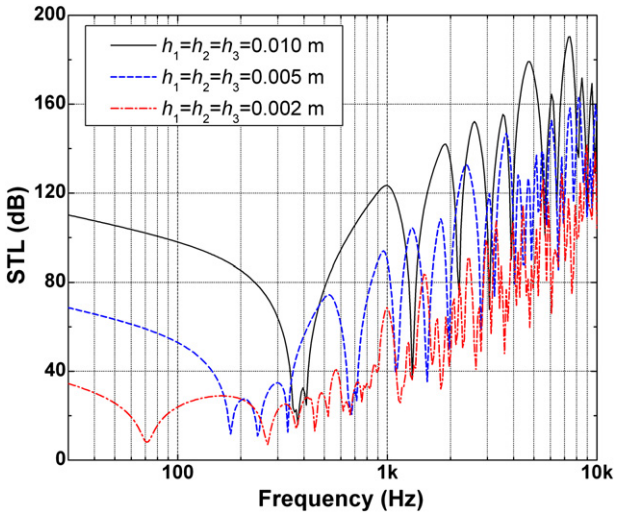

Fig. 9. Effects of panel thickness on STL for finite triple-panel partition (0.5 m × 0.5 m, $\tilde{H}_1 = \tilde{H}_2 = 0.01$ m) under normal sound excitation.

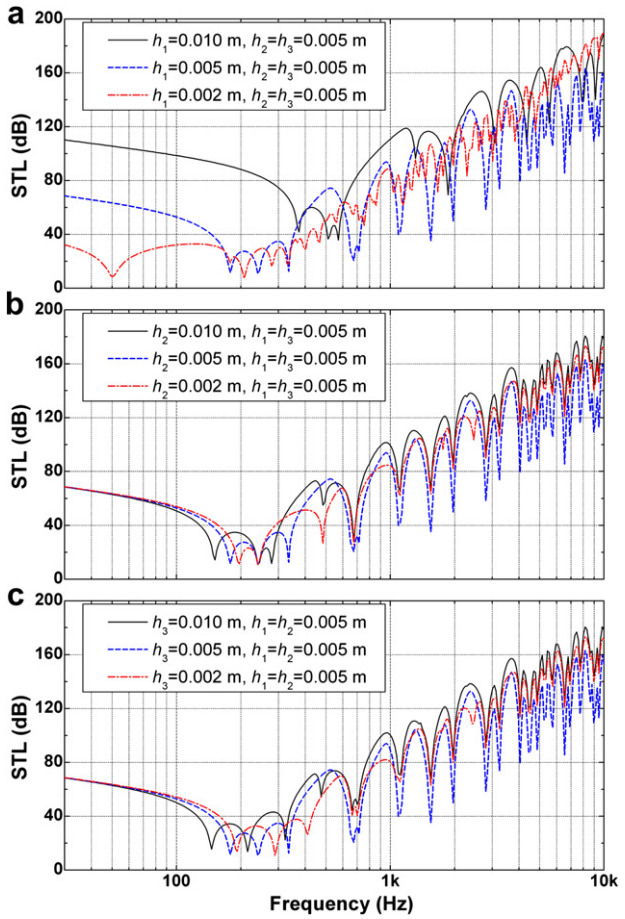

Fig. 10. Variation of *STL* for finite triple-panel partition (0.5 m × 0.5 m, $\bar{H}_1 = \bar{H}_2 = 0.01$ m) under normal sound excitation with the thickness of: (a) incident panel; (b) middle panel; (c) radiation panel.

For triple-panel partitions of finite extent, as the panel thickness is increased, two prominent features can be observed from Fig. 9: (1) remarkable increase of the *STL* value; (2) shifting of the resonance dips toward higher frequencies, which is attributed to the increased panel stiffness and surface density. The individual role of each panel in sound transmission is illustrated in Fig. 10(a–c) for the incident panel, the middle panel and the radiation panel, respectively. The most noticeable feature of the results shown in Fig. 10 is that increasing the incident panel thickness causes the STL value to increase more dramatically than increasing the thickness of the middle or radiation panel, especially at relatively low frequencies. This is because the middle or radiation panel does not significantly affect the coupling between the panels through air stiffness for frequencies below the cut-off frequency of the cavities (Brekke, 1981). This feature is also consistent with the experimental

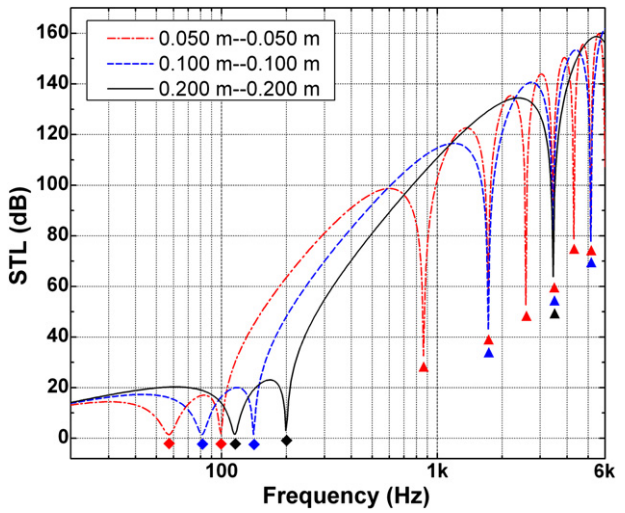

Fig. 11. Effects of air cavity thickness on STL for infinite triple-panel partition ($h_1^t = h_2^t = h_3^t = 0.002$ m) under normal sound excitation: ◆ mass–air–mass–air–mass resonance; ▲ standing-wave resonance.

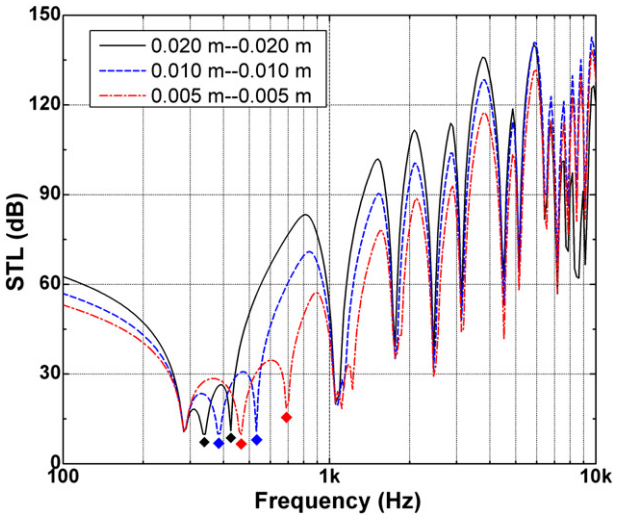

Fig. 12. Effects of air cavity thickness on STL for finite triple-panel partition (0.25 m × 0.25 m, $h_1^t = h_2^t = h_3^t = 0.002$ m) under normal sound excitation: ◆ mass–air–mass–air–mass resonance.

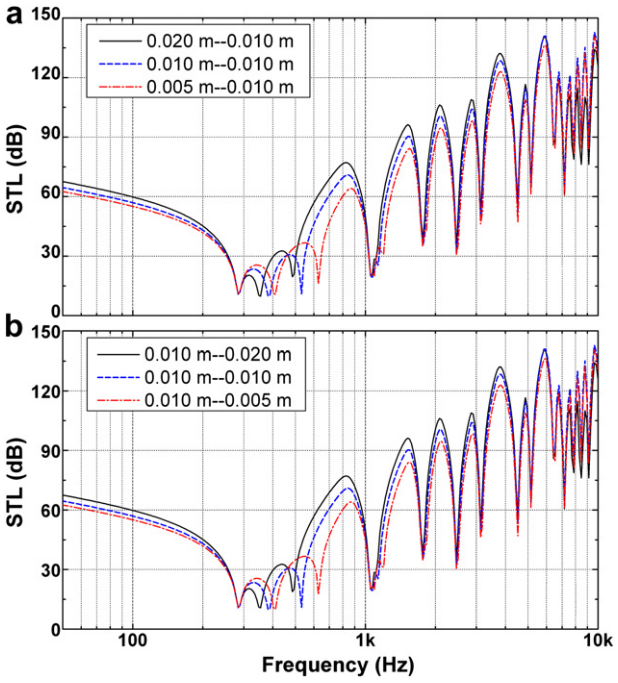

Fig. 13. Effects of air cavity thickness on STL for finite triple-panel partition (0.25 m × 0.25 m, $h_1^t = h_2^t = h_3^t = 0.002$ m) partition under normal sound excitation: (a) only varying the depth of the air cavity adjacent to the incident panel; (b) only varying the depth of the air cavity adjacent to the radiating panel.

results of (Vinokur, 1990). The pronounced deviation between the resonant dips for different cases shown in Fig. 10(a) implies the predominant role of the incident panel vibratory modes. In contrast, the good agreement between the resonant dips in the high frequency range for different panel thicknesses in Fig. 10(b and c) suggests that the vibratory modes of the middle or radiation panel have negligible effects. At relatively low frequencies, however, the shifting of the resonant dips with varying panel thickness demonstrates the significant effects of each panel [see Fig. 10(a–c)]. Note that the steeper dips for the case of ($h_1^t = h_2^t = h_3^t = 0.005$ m) than other cases is attributed to the noticeable enhancement of the same vibratory modes of the three identical panels.

3.3.3. *Effects of air cavity depth*

For an infinitely large triple-panel partition under normal sound excitation, Fig. 11 plots the STL versus frequency curves for selected air cavity depths, with the thickness of each panel fixed at 0.002 m. As the air cavity depth is increased, the tendency of the STL versus frequency curve varies significantly. Within the frequency range between the mass-spring resonance and the first order standing-wave resonance, increasing the air cavity depth leads to remarkable increase of the STL value. The mass-spring resonance dips shift downward with increasing air cavity depth, which is attributed to the decreased equivalent stiffness of the air cavities. According to Eq. (41), the natural frequency of each standing-wave resonance decreases as the air cavity depth is increased, which is consistent with the results of Fig. 11.

The effects of air cavity depth on sound transmission across a finite-sized triple-panel partition are shown in Figs. 12 and 13, again with the panel thickness fixed at 0.002 m. It is seen that whilst the increase of air cavity depth leads to enhanced soundproofing capability of the structure, the effects are particularly noticeable if the depth of the two cavities is increased simultaneously (see Fig. 12). The mass-spring resonance dips alter significantly, consistent with the predictions of Eqs. (39) and (40). The dips dominated by panel vibratory modes change little because the boundary condition plays a stronger effect than cavity coupling effects at these dips. In addition, the good agreement between Fig. 13(a and b) demonstrates the identical role of the two air cavities in the process of sound transmission through the finite triple-panel structure, which can be explained with the acoustical reciprocal theorem.

4. Concluding remarks

A theory has been established that can be used to predict the sound transmission characteristics of a clamp mounted triple-panel partition separated by two enclosed air cavities. A set of modal functions (basic functions) are employed to account for the clamped boundary conditions, and the application of the virtual work principle leads to a set of simultaneous algebraic equations for determining the unknown modal coefficients. The present theory has the advantage of clearly showing the major vibroacoustic phenomena associated with the edge constraints and fluid–structure coupling, such as the equivalent mass-spring resonance, the standing-wave resonance and the modal resonance of the system. Extensive numerical calculations are carried out to obtain the frequency characteristic curves of the transmission loss performance of the triple-panel structure, with detailed physical explanations given for the above mentioned resonance dips. Comparison of the triple-panel partition with the double-panel partition suggests that, for the purpose of maximizing the transmission loss, the former is a preferred alternative of the latter although the superiority is not remarkable when the total masses of the two are equivalent. Moreover, the relatively large number of system parameters owned by the triple-panel partition allows more design space for tailoring its noise reduction capability. Since for many applications, noise reduction at the low-frequency range (<500 Hz) is of vital importance, the finding that the soundproofing capability of a triple-panel partition increases with decreasing panel dimensions has significant implications on the design of soundproofing windows installed in high-class buildings and aircraft fuselages.

As a future work, an active control strategy to minimize the sound transmission across a clamp mounted triple-panel structure will be analytically and experimentally developed based upon the proposed theory from the viewpoint of practical noise reduction.

Acknowledgments

This work is supported by the National Basic Research Program of China (2011CB610300), the National 111 Project of China (B06024), the National Natural Science Foundation of China (11072188 and 10825210) and the Shaanxi Province 13115 project (S2010ZDKG704).

Appendix A. Modal coefficients and generalized forces

The modal coefficients of the three panels are:

$$\{\boldsymbol{\alpha}_1\} = \begin{bmatrix} \alpha_{1,11} & \alpha_{1,21} & \cdots & \alpha_{1,M1} & \alpha_{1,12} & \alpha_{1,22} & \cdots \\ & \alpha_{1,M2} & \cdots & \alpha_{1,MN} & & & \end{bmatrix}^T_{MN\times 1} \tag{A1}$$

$$\{\boldsymbol{\alpha}_2\} = \begin{bmatrix} \alpha_{2,11} & \alpha_{2,21} & \cdots & \alpha_{2,M1} & \alpha_{2,12} & \alpha_{2,22} & \cdots \\ & \alpha_{2,M2} & \cdots & \alpha_{2,MN} & & & \end{bmatrix}^T_{MN\times 1} \tag{A2}$$

$$\{\boldsymbol{\alpha}_3\} = \begin{bmatrix} \alpha_{3,11} & \alpha_{3,21} & \cdots & \alpha_{3,M1} & \alpha_{3,12} & \alpha_{3,22} & \cdots \\ & \alpha_{3,M2} & \cdots & \alpha_{3,MN} & & & \end{bmatrix}^T_{MN\times 1} \tag{A3}$$

The generalized forces can be written in vector form as:

$$\{\mathbf{F}\} = 2j\omega\rho_0 I[f_{11}\ f_{21}\ \cdots\ f_{M1}\ f_{12}\ f_{22}\ \cdots\ f_{M2}\ \cdots\ f_{MN}]^T_{MN\times 1} \tag{A4}$$

$$\lambda^{*1}_{1,mn} = 3\left(\frac{m}{a}\right)^4 + 3\left(\frac{n}{b}\right)^4 + 2\left(\frac{m}{a}\right)^2\left(\frac{n}{b}\right)^2 \tag{A5}$$

$$\Delta_1^{*1} = \begin{bmatrix} \lambda^{*1}_{1,11} & & & & & & & & & \\ & \lambda^{*1}_{1,21} & & & & & & & & \\ & & \ddots & & & & & & & \\ & & & \lambda^{*1}_{1,M1} & & & & & & \\ & & & & \lambda^{*1}_{1,12} & & & & & \\ & & & & & \lambda^{*1}_{1,22} & & & & \\ & & & & & & \ddots & & & \\ & & & & & & & \lambda^{*1}_{1,M2} & & \\ & & & & & & & & \ddots & \\ & & & & & & & & & \lambda^{*1}_{1,MN} \end{bmatrix}_{MN\times MN} \tag{A6}$$

$$\lambda^{*2}_{1,n} = \frac{2n^4}{b^4}\begin{bmatrix} 0 & 1 & 1 & \cdots & 1 \\ 1 & 0 & 1 & \cdots & 1 \\ 1 & 1 & 0 & \cdots & \cdots \\ \cdots & \cdots & \cdots & \ddots & 1 \\ 1 & 1 & \cdots & 1 & 0 \end{bmatrix}_{M\times N} \tag{A7}$$

$$\Delta_1^{*2} = \begin{bmatrix} \lambda_{1,1}^{*2} & & & \\ & \lambda_{1,2}^{*2} & & \\ & & \ddots & \\ & & & \lambda_{1,N}^{*2} \end{bmatrix}_{MN\times MN} \tag{A8}$$

$$\lambda_1^{*3} = \frac{2}{a^4}\begin{bmatrix} 1^4 & & & \\ & 2^4 & & \\ & & \ddots & \\ & & & M^4 \end{bmatrix}_{M\times N} \tag{A9}$$

$$\Delta_1^{*3} = \begin{bmatrix} 0 & \lambda_1^{*3} & \lambda_1^{*3} & \cdots & \lambda_1^{*3} \\ \lambda_1^{*3} & 0 & \lambda_1^{*3} & \cdots & \lambda_1^{*3} \\ \lambda_1^{*3} & \lambda_1^{*3} & 0 & \cdots & \cdots \\ \cdots & \cdots & \cdots & \ddots & \lambda_1^{*3} \\ \lambda_1^{*3} & \lambda_1^{*3} & \cdots & \lambda_1^{*3} & 0 \end{bmatrix}_{MN\times MN} \tag{A10}$$

$$\Delta_2^{*1} = \frac{9ab}{4}\begin{bmatrix} 1 & & & \\ & 1 & & \\ & & \ddots & \\ & & & 1 \end{bmatrix}_{MN\times MN} \tag{A11}$$

$$\lambda_2^{*2} = \frac{3ab}{2}\begin{bmatrix} 0 & 1 & 1 & \cdots & 1 \\ 1 & 0 & 1 & \cdots & 1 \\ 1 & 1 & 0 & \cdots & \cdots \\ \cdots & \cdots & \cdots & \ddots & 1 \\ 1 & 1 & \cdots & 1 & 0 \end{bmatrix}_{M\times N} \tag{A12}$$

$$\Delta_2^{*2} = \begin{bmatrix} \lambda_2^{*2} & & & \\ & \lambda_2^{*2} & & \\ & & \ddots & \\ & & & \lambda_2^{*2} \end{bmatrix}_{MN\times MN} \tag{A13}$$

$$\lambda_2^{*3} = \frac{3ab}{2}\begin{bmatrix} 1 & & & \\ & 1 & & \\ & & \ddots & \\ & & & 1 \end{bmatrix}_{M\times N} \tag{A14}$$

$$\Delta_2^{*3} = \begin{bmatrix} 0 & \lambda_2^{*3} & \lambda_2^{*3} & \cdots & \lambda_2^{*3} \\ \lambda_2^{*3} & 0 & \lambda_2^{*3} & \cdots & \lambda_2^{*3} \\ \lambda_2^{*3} & \lambda_2^{*3} & 0 & \cdots & \cdots \\ \cdots & \cdots & \cdots & \ddots & \lambda_2^{*3} \\ \lambda_2^{*3} & \lambda_2^{*3} & \cdots & \lambda_2^{*3} & 0 \end{bmatrix}_{MN\times MN} \tag{A15}$$

$$\lambda_2^{*4} = ab\begin{bmatrix} 0 & 1 & 1 & \cdots & 1 \\ 1 & 0 & 1 & \cdots & 1 \\ 1 & 1 & 0 & \cdots & \cdots \\ \cdots & \cdots & \cdots & \ddots & 1 \\ 1 & 1 & \cdots & 1 & 0 \end{bmatrix}_{M\times N} \tag{A16}$$

$$\Delta_2^{*4} = \begin{bmatrix} 0 & \lambda_2^{*4} & \lambda_2^{*4} & \cdots & \lambda_2^{*4} \\ \lambda_2^{*4} & 0 & \lambda_2^{*4} & \cdots & \lambda_2^{*4} \\ \lambda_2^{*4} & \lambda_2^{*4} & 0 & \cdots & \cdots \\ \cdots & \cdots & \cdots & \ddots & \lambda_2^{*4} \\ \lambda_2^{*4} & \lambda_2^{*4} & \cdots & \lambda_2^{*4} & 0 \end{bmatrix}_{MN\times MN} \tag{A17}$$

In the context of the above sub-matrices, the elemental matrices can be derived as:

$$[\mathbf{T}_{11}]_{MN\times MN} = 4D_1\pi^4 ab\left(\Delta_1^{*1} + \Delta_1^{*2} + \Delta_1^{*3}\right) - \left(m_1\omega^2 + j\omega\rho_0\frac{2\omega e^{2jk_zH_1}}{k_z\left(1-e^{2jk_zH_1}\right)}\right)\cdot\left(\Delta_2^{*1} + \Delta_2^{*2} + \Delta_2^{*3} + \Delta_2^{*4}\right) \tag{A18}$$

$$[\mathbf{T}_{12}]_{MN\times MN} = j\omega\rho_0\frac{2\omega e^{jk_zH_1}}{k_z\left(1-e^{2jk_zH_1}\right)}\left(\Delta_2^{*1} + \Delta_2^{*2} + \Delta_2^{*3} + \Delta_2^{*4}\right) \tag{A19}$$

$$[\mathbf{T}_{21}]_{MN\times MN} = j\omega\rho_0\frac{2\omega e^{jk_zH_1}}{k_z\left(1-e^{2jk_zH_1}\right)}\left(\Delta_2^{*1} + \Delta_2^{*2} + \Delta_2^{*3} + \Delta_2^{*4}\right) \tag{A20}$$

$$[\mathbf{T}_{22}]_{MN\times MN} = 4D_2\pi^4 ab\left(\Delta_1^{*1} + \Delta_1^{*2} + \Delta_1^{*3}\right) + \left(-m_2\omega^2 + \frac{\omega^2\rho_0\left(e^{jk_z(H_1-H_2)} - e^{jk_z(H_1+H_2)}\right)}{k_z\left(-1+e^{2jk_zH_1}\right)\sin\left(k_z(H_1-H_2)\right)}\right)\left(\Delta_2^{*1} + \Delta_2^{*2} + \Delta_2^{*3} + \Delta_2^{*4}\right) \tag{A21}$$

$$[\mathbf{T}_{23}]_{MN\times MN} = \frac{\omega^2\rho_0}{k_z\sin\left(k_z(H_1-H_2)\right)}\left(\Delta_2^{*1} + \Delta_2^{*2} + \Delta_2^{*3} + \Delta_2^{*4}\right) \tag{A22}$$

$$[\mathbf{T}_{32}]_{MN\times MN} = \frac{\omega^2\rho_0}{k_z\sin\left(k_z(H_1-H_2)\right)}\left(\Delta_2^{*1} + \Delta_2^{*2} + \Delta_2^{*3} + \Delta_2^{*4}\right) \tag{A23}$$

$$[\mathbf{T}_{33}]_{MN\times MN} = 4D_3\pi^4 ab\left(\Delta_1^{*1} + \Delta_1^{*2} + \Delta_1^{*3}\right) - \left(m_3\omega^2 + \frac{\omega^2\rho_0 e^{-jk_z(H_1-H_2)}}{k_z\ \sin\ \left(k_z(H_1-H_2)\right)}\right)\times\left(\Delta_2^{*1} + \Delta_2^{*2} + \Delta_2^{*3} + \Delta_2^{*4}\right) \tag{A24}$$

References

Antonio, J.M.P., Tadeu, A., Godinho, L., 2003. Analytical evaluation of the acoustic insulation provided by double infinite walls. Journal of Sound and Vibration 263, 113–129.

Beranek, L.L., Work, G.A., 1949. Sound transmission through multiple structures containing flexible blankets. Journal of the Acoustical Society of America 21, 419–428.

Brekke, A., 1981. Calculation methods for the transmission loss of single, double and triple partitions. Applied Acoustics 14, 225–240.

Carneal, J.P., Fuller, C.R., 2004. An analytical and experimental investigation of active structural acoustic control of noise transmission through double panel systems. Journal of Sound and Vibration 272, 749–771.

Chazot, J.D., Guyader, J.L., 2007. Prediction of transmission loss of double panels with a patch-mobility method. Journal of the Acoustical Society of America 121, 267–278.

Craik, R.J.M., 2003. Non-resonant sound transmission through double walls using statistical energy analysis. Applied Acoustics 64, 325–341.

Del Coz Diaz, J.J., Alvarez Rabanal, F.P., Garcia Nieto, P.J., Serrano Lopez, M.A., 2010. Sound transmission loss analysis through a multilayer lightweight concrete hollow brick wall by fem and experimental validation. Building and Environment 45, 2373–2386.

Fahy, F., 1985. Sound and Structural Vibration: Radiation, Transmission and Response. Academic Press, London.

Fahy, F.J., 1994. Statistical energy analysis: a critical overview. Philosophical Transactions: Physical Sciences and Engineering 346, 431–447.

Gardonio, P., 2002. Review of active techniques for aerospace vibro-acoustic control. Journal of Aircraft 39, 206–214.

Gardonio, P., Elliott, S.J., 1999. Active control of structure-borne and airborne sound transmission through double panel. Journal of Aircraft 36, 1023–1032.

Graham, W.R., 2007. Analytical approximations for the modal acoustic impedances of simply supported, rectangular plates. Journal of the Acoustical Society of America 122, 719–730.

Ingard, U., 1959. Influence of fluid motion past a plane boundary on sound reflection, absorption, and transmission. Journal of the Acoustical Society of America 31, 1035–1036.
Kaiser, O.E., Pietrzko, S.J., Morari, M., 2003. Feedback control of sound transmission through a double glazed window. Journal of Sound and Vibration 263, 775–795.
Langley, R.S., Smith, J.R.D., Fahy, F.J., 1997. Statistical energy analysis of periodically stiffened damped plate structures. Journal of Sound and Vibration 208, 407–426.
Lee, J.H., Kim, J., 2002. Analysis of sound transmission through periodically stiffened panels by space-harmonic expansion method. Journal of Sound and Vibration 251, 349–366.
Leissa, A.W., 1993. Vibrations of plates. Acoustical Society of America.
Leppington, F.G., Broadbent, E.G., Butler, G.F., 2006. Transmission of sound through a pair of rectangular elastic plates. IMA Journal of Applied Mathematics 71, 940–955.
Lin, G.-F., Garrelick, J.M., 1977. Sound transmission through periodically framed parallel plates. Journal of the Acoustical Society of America 61, 1014–1018.
Liu, B., Feng, L., Nilsson, A., 2007. Sound transmission through curved aircraft panels with stringer and ring frame attachments. Journal of Sound and Vibration 300, 949–973.
Lomas, N.S., Hayek, S.I., 1977. Vibration and acoustic radiation of elastically supported rectangular plates. Journal of Sound and Vibration 52, 1–25.
London, A., 1950. Transmission of reverberant sound through double walls. Journal of the Acoustical Society of America 22, 270–279.
Lyle, K., Mixson, J., 1987. Laboratory study of sidewall noise transmission and treatment for a light aircraft fuselage. Journal of Aircraft 24, 660–665.
Maidanik, G., 1962. Response of ribbed panels to reverberant acoustic fields. The Journal of the Acoustical Society of America 34, 809–826.
Mulholland, K.A., Price, A.J., Parbrook, H.D., 1968. Transmission loss of multiple panels in a random incidence field. Journal of the Acoustical Society of America 43, 1432–1435.
Panneton, R., Atalla, N., 1996. Numerical prediction of sound transmission through finite multilayer systems with poroelastic materials. Journal of the Acoustical Society of America 100, 346–354.
Pellicier, A., Trompette, N., 2007. A review of analytical methods, based on the wave approach, to compute partitions transmission loss. Applied Acoustics 68, 1192–1212.
Pietrzko, S.J., Mao, Q., 2008. New results in active and passive control of sound transmission through double wall structures. Aerospace Science and Technology 12, 42–53.
Price, A.J., Crocker, M.J., 1970. Sound transmission through double panels using statistical energy analysis. Journal of the Acoustical Society of America 47, 683–693.
Quirt, J.D., 1982. Sound transmission through windows i. Single and double glazing. Journal of the Acoustical Society of America 72, 834–844.
Quirt, J.D., 1983. Sound transmission through windows ii. Double and triple glazing. Journal of the Acoustical Society of America 74, 534–542.
Ruzzene, M., 2004. Vibration and sound radiation of sandwich beams with honeycomb truss core. Journal of Sound and Vibration 277, 741–763.
Sas, P., Bao, C., Augusztinovicz, F., Desmet, W., 1995. Active control of sound transmission through a double panel partition. Journal of Sound and Vibration 180, 609–625.
Sewell, E.C., 1970. Transmission of reverberant sound through a single-leaf partition surrounded by an infinite rigid baffle. Journal of Sound and Vibration 12, 21–32.
Sgard, F.C., Atalla, N., Nicolas, J., 2000. A numerical model for the low frequency diffuse field sound transmission loss of double-wall sound barriers with elastic porous linings. Journal of the Acoustical Society of America 108, 2865–2872.
Tadeu, A.J.B., Mateus, D.M.R., 2001. Sound transmission through single, double and triple glazing. Experimental evaluation. Applied Acoustics 62, 307–325.
Taylor, R.L., Govindjee, S., 2004. Solution of clamped rectangular plate problems. Communications in Numerical Methods in Engineering 20, 757–765.
Toyoda, M., Kugo, H., Shimizu, T., Takahashi, D., 2008. Effects of an air-layer-subdivision technique on the sound transmission through a single plate. Journal of the Acoustical Society of America 123, 825–831.
Villot, M., Guigou, C., Gagliardini, L., 2001. Predicting the acoustical radiation of finite size multi-layered structures by applying spatial windowing on infinite structures. Journal of Sound and Vibration 245, 433–455.
Vinokur, R.Y., 1990. Transmission loss of triple partitions at low frequencies. Applied Acoustics 29, 15–24.
Wang, J., Lu, T.J., Woodhouse, J., Langley, R.S., Evans, J., 2005. Sound transmission through lightweight double-leaf partitions: theoretical modelling. Journal of Sound and Vibration 286, 817–847.
Wu, S.F., Wu, G., Puskarz, M.M., Gleason, M.E., 1997. Noise transmission through a vehicle side window due to turbulent boundary layer excitation. Journal of Vibration and Acoustics 119, 557–562.
Xin, F.X., Lu, T.J., 2009. Analytical and experimental investigation on transmission loss of clamped double panels: Implication of boundary effects. Journal of the Acoustical Society of America 125, 1506–1517.
Xin, F.X., Lu, T.J., 2010a. Analytical modeling of fluid loaded orthogonally rib-stiffened sandwich structures: sound transmission. Journal of the Mechanics and Physics of Solids 58, 1374–1396.
Xin, F.X., Lu, T.J., 2010b. Analytical modeling of sound transmission across finite aeroelastic panels in convected fluids. Journal of the Acoustical Society of America 128, 1097–1107.
Xin, F.X., Lu, T.J., 2010c. Sound radiation of orthogonally rib-stiffened sandwich structures with cavity absorption. Composites Science and Technology 70, 2198–2206.
Xin, F.X., Lu, T.J., 2011a. Analytical modeling of wave propagation in orthogonally rib-stiffened sandwich structures: sound radiation. Computers and Structures 89, 507–516.
Xin, F.X., Lu, T.J., 2011b. Transmission loss of orthogonally rib-stiffened double-panel structures with cavity absorption. Journal of the Acoustical Society of America 129, 1919–1934.
Xin, F.X., Lu, T.J., Chen, C.Q., 2008. Vibroacoustic behavior of clamp mounted double-panel partition with enclosure air cavity. The Journal of the Acoustical Society of America 124, 3604–3612.
Xin, F.X., Lu, T.J., Chen, C.Q., 2009a. Dynamic response and acoustic radiation of double-leaf metallic panel partition under sound excitation. Computational Materials Science 46, 728–732.
Xin, F.X., Lu, T.J., Chen, C.Q., 2009b. External mean flow influence on noise transmission through double-leaf aeroelastic plates. AIAA Journal 47, 1939–1951.
Xin, F.X., Lu, T.J., Chen, C.Q., 2010. Sound transmission through simply supported finite double-panel partitions with enclosed air cavity. Journal of Vibration and Acoustics 132 (011008), 1–11.
Yairi, M., Sakagami, K., Morimoto, M., Minemura, A., Andow, K., 2003. Effect of acoustical damping with a porous absorptive layer in the cavity to reduce the structure-borne sound radiation from a double-leaf structure. Applied Acoustics 64, 365–384.